

Quasi-periodic injections of relativistic electrons in Saturn's outer magnetosphere



E. Roussos^{a,*}, N. Krupp^a, D.G. Mitchell^b, C. Paranicas^b, S.M. Krimigis^b, M. Andriopoulou^c, B. Palmaerts^{a,g}, W.S. Kurth^d, S.V. Badman^e, A. Masters^f, M.K. Dougherty^f

^a Max Planck Institute for Solar System Research, Justus-von-Liebig-Weg 3, 37077 Göttingen, Germany

^b Johns Hopkins University Applied Physics Laboratory, 11100 Johns Hopkins Road, Laurel, MD 20723-6099, USA

^c Space Science Research Institute, Austrian Academy of Science, Schmiedlstrasse 6, 8042 Graz, Austria

^d Department of Physics and Astronomy, University of Iowa, Iowa City, IA 52242-1479, USA

^e Lancaster University, Bailrigg, Lancaster LA1 4YB, UK

^f Space and Atmospheric Physics Group, The Blackett Laboratory, Imperial College London, Prince Consort Road, London SW7 2AZ, UK

^g Laboratoire de Physique Atmosphérique et Planétaire, Université de Liège, Liège, Belgium

ARTICLE INFO

Article history:

Received 18 July 2014

Revised 30 March 2015

Accepted 11 April 2015

Available online 28 April 2015

Keywords:

Magnetospheres

Saturn, magnetosphere

Aurorae

ABSTRACT

Quasi-periodic, short-period injections of relativistic electrons have been observed in both Jupiter's and Saturn's magnetospheres, but understanding their origin or significance has been challenging, primarily due to the limited number of in-situ observations of such events by past flyby missions. Here we present the first survey of such injections in an outer planetary magnetosphere using almost nine years of energetic charged particle and magnetic field measurements at Saturn. We focus on events with a characteristic period of about 60–70 min (QP60, where QP stands for quasi-periodic). We find that the majority of QP60, which are very common in the outer magnetosphere, map outside Titan's orbit. QP60 are also observed over a very wide range of local times and latitudes. A local time asymmetry in their distribution is the most striking feature, with QP60 at dusk being between 5 and 25 times more frequent than at dawn. Field-line tracing and pitch angle distributions suggest that most events at dusk reside on closed field lines. They are distributed either near the magnetopause, or, in the case of the post-dusk (or pre-midnight) sector, up to about 30 R_S inside it, along an area extending parallel to the dawn–dusk direction. QP60 at dawn map either on open field lines and/or near the magnetopause. Both the asymmetries and varying mapping characteristics as a function of local time indicate that generation of QP60 cannot be assigned to a single process. The locations of QP60 seem to trace sites that reconnection is expected to take place. In that respect, the subset of events observed post-dusk and deep inside the magnetopause may be directly or indirectly linked to the Vasyliunas reconnection cycle, while magnetopause reconnection/Kelvin–Helmholtz (KH) instability could be invoked to explain all other events at the dusk-side. Using similar arguments, injections at the dawnside magnetosphere may result from solar-wind induced storms and/or magnetopause reconnection/KH-instability. Still, we cannot exclude that the apparent collocation of QP60 with expected reconnection sites is coincidental, given also the large uncertainties in field line tracing with the available magnetic field models. The intensity of the QP60 spectrum is strong enough such that if transport processes allow, these injections can be a very important source of energetic electrons for the inner saturnian magnetosphere or the heliosphere. We also observe that electrons in a QP60 can be accelerated at least up to 6 MeV and that the distribution of QP60 appears to trace well the aurora's local time structure, an observation that may have implications about high-latitude electron acceleration and the connection of these events to auroral dynamics. Despite these new findings, it is still unclear what determines the rather well-defined 60 to 70-min period of the electron bursts and how electrons can rapidly reach several MeV.

© 2015 Elsevier Inc. All rights reserved.

1. Introduction

Relativistic electrons have been detected in all planetary magnetospheres of our Solar System with the highest intensities

* Corresponding author.

E-mail address: roussos@mps.mpg.de (E. Roussos).

observed within the boundaries of the stable charged particle trapping regions, that is the radiation belts (Mauk and Fox, 2010). The source (or seed) electron population of the belts resides typically within the middle or outer magnetosphere and its energy spectrum extends up to few hundred keV or several MeV, depending on the planet. Acceleration of this population by one or more processes (adiabatic transport, wave–particle interactions, flux-tube interchange, solar-wind transients) may give rise to the high intensities of MeV electrons observed within the belts (Shprits et al., 2012; Paranicas et al., 2010; Gannon et al., 2005; Horne et al., 2005; de Pater, 1981; Lyons and Thorne, 1973).

What is, however, less clear is how the high numbers and energies of the seed electrons are derived. At Earth, dipolarization associated injections and convection changes have been shown to be sufficient to supply the MeV electron population in the outer belt, at least on certain instances. Similarly at Saturn, it is believed that dipolarizations play a key role in supporting the at least part of the seed electron population, but it has not yet been demonstrated if their occurrence fully justifies the large energies and/or intensities in the middle magnetosphere. For example, Mitchell et al. (2015) discusses several examples of Cassini observations with recently injected energetic particle populations in the middle magnetosphere of Saturn. Peak electron energies in one such example (day 301/2004) are at about 200 keV on a background population that extends at least up to 800 keV in this specific case or to about 1 MeV on average (Kollmann et al., 2011). It is therefore important to evaluate the relative importance of additional sources in providing energetic electrons to the middle magnetosphere and, eventually, the radiation belt.

One such source may be a type of quasi-periodic energetic electron injections, first reported by Schardt et al. (1985) using Voyager-2 observations in the dawn sector of Saturn's magnetosphere and at intermediate latitudes ($\sim 29^\circ$). The signature of each of these injections was a sudden increase of energetic electron intensities (by 1–2 orders of magnitude) in the energy range of 100 keV to several MeV, followed by a slower, exponential decay that lasted between 30 and 60 min (“sawtooth” structure). Each injection involved two or more of these sawteeth repeated at quasi-regular intervals of 40–80 min. As Voyager-2 was a flyby mission it remained unclear how common such events were or what their spatial distribution was, despite the authors noting the highly unusual interplanetary conditions during the flyby.

Quasi-periodic injections have also been reported in recent publications based on Cassini observations. Mitchell et al. (2009) described such an event from day 269 of 2006, highlighting also how the coincident signatures in energetic ion, plasma wave and magnetic field measurements are similar to those of downward sheet currents in Earth's auroral zone. This event took place at intermediate latitudes, but at the post-dusk sector of the magnetosphere, far from the location of the Voyager-2 observations. Its position also mapped relatively deep inside the magnetopause. Badman et al. (2012) reported a similar event from day 320 of 2008, where the recurrent electron injections extended down to energies of few tens of keV. This observation took place around local noon and at high, north latitudes. The authors attributed the enhanced electron intensities to scattered electrons in downward current regions that map into transient structures in Saturn's aurora that are triggered by reconnection. Masters et al. (2010) observed also a quasi-periodic electron signature coincident with a vortex structure in the pre-noon sector of Saturn's outer magnetosphere. This vortex was associated to the growth of the Kelvin–Helmholtz (KH) instability at the magnetopause, a flow-shear instability that can also trigger reconnection in planetary magnetospheres.

While both aforementioned Cassini and Voyager-2 studies focused on single case events, it is evident that these sawtooth

electron injections may be taking place globally in Saturn's magnetosphere. Besides being a potentially important source of relativistic electrons, the evidence suggesting that they may be originating at reconnection sites may also make them an important tracer of that process. What is also interesting is that strikingly similar type of quasi-periodic electron injections were seen during Ulysses's flyby of Jupiter with a period in the 40–80 min range. Radio emissions that appear to have a common origin with the aforementioned electron injections at Jupiter (McKibben et al., 1993; MacDowall et al., 1993; Zhang et al., 1995) were also detected. This suggests that quasi-periodic electron injections may be connected to fundamental dynamical processes in corotation-dominated magnetospheres.

Here we take advantage of Cassini's extended tour of the saturnian system to derive for the first time statistical properties of these quasi-periodic electron injections in an outer planet's magnetosphere. While numerous aspects of these injections can be investigated, for this initial study we will focus mostly on their spatial nature. Spectral, angular electron distribution characteristics and the response of the magnetic field is also explored briefly. We will use these data in order to constrain the physical origin of the injections and to understand their relation to trapped electron populations in Saturn's middle magnetosphere. This work also provides important context for a series of studies that report, similar, short period quasi-periodic pulsations in in-situ and auroral data obtained during the 2013 Saturn Aurora Campaign (Badman et al., 2016; Mitchell et al., 2016).

2. Instrumentation and analysis tools

Most of the data presented in this study are from Cassini's MIMI/LEMMS energetic charged particle detector (Krimigis et al., 2004). LEMMS has two telescopes pointing in opposite directions, called the Low Energy and the High Energy Telescope (LET/HET respectively). Each telescope contains different type of channels for separating the species (ions/electrons) and for constraining the energy of the measured particles with different time and energy resolution.

The channel types used here are the “rate” and the “pulse-height-analysis (PHA)” channels. The former have the advantage of a good geometric factor for both the keV and the MeV range, a wide energy coverage (electron energies from about 20 keV to greater than 10 MeV) and the use of coincidence techniques which can partly suppress penetrating particles and light contamination. The disadvantage of the rate channels is the moderate or poor energy resolution at the MeV range ($\Delta E/E > 1$). The PHA channels achieve an energy resolution between 0.06 and 0.07 for the energy range of 25 keV and 1.6 MeV at the expense of a lower sensitivity and the lack of coincidence measurements. For these reasons, the use of rate and PHA channels is complementary.

More specifically, we analyzed data from electron rate channels C0–C7 (LET: 18–532 keV) and E0–E7 (HET: >95 keV). Although the magnetospheric structures analyzed appear in electrons, we also review energetic ion data for the context, since also Mitchell et al. (2009) and Zhang et al. (1995) report coincident field-aligned structures in proton intensities. Ion rate channels considered here are A0–A7 and P2 (27–4920 keV). Regarding the electron PHA channels, we mostly use the ones above 250 keV (PHA-F1 detector) in order to constrain the energy spectral shape beyond about 1 MeV, where energy resolution is poor. The signal from lower energy PHAs (PHA-E detector) can be very sensitive to light contamination, affecting the results of spectral form fits to the data. The LEMMS signal is corrected for the instrumental background as described in previous papers (Roussos et al., 2011;

Kollmann et al., 2011). Passband information for the rate channels is available in Krupp et al. (2009). All LEMMS data were averaged in an 86-s resolution, which is the duration of one of LEMMS's sampling cycles. The typical time resolution is about 5 s so this averaging improves considerably the signal to noise ratio.

Particle pitch angles are calculated using information on the LEMMS pointing and the magnetic field orientation from Cassini's magnetometer (MAG) (Dougherty et al., 2004). For most of the studied period the pitch angle pointing of LEMMS depends solely on the attitude of Cassini and pitch angle distributions may only be obtained when the spacecraft is rolling. For periods before the 2nd of February of 2005, pitch angle distributions are more regularly available as LEMMS's scan platform was functional. Magnetometer data are also reviewed for identifying coincident features with the quasi-periodic electron injections that we study here.

Since the features we analyze are found in Saturn's outer magnetosphere, we use the Khurana et al. (2006) magnetic field model (K06) to map their location to either the planet or the equatorial plane. The model is based on that of Khurana (1997) for Jupiter (internal field plus current sheet perturbation), but in addition includes magnetopause and tail fields. Its output depends mostly on the solar wind dynamic pressure. While this version of the model has limitations, it is the only one available to us that can describe the global shape of the magnetospheric field.

3. 60 to 70-min, quasi-periodic electron injections (QP60)

Our review covers the period between June 28 of 2004 (180/2004) until May 7th of 2013 (124/2013). During that interval Cassini sampled extensively most domains of the saturnian magnetosphere over a wide range of distances, local times and latitudes, providing the necessary coverage for the purposes of our study.

3.1. Examples

We now present several characteristic examples of the pulsed events in Figs. 1–5. The purpose of showing the examples below is to illustrate some of the varying characteristics of the quasi-periodic events that went in our statistical sample (Section 3.2). All figures have similar structure, which we describe below using Fig. 1 for reference.

Fig. 1 has a stack of panels on the left containing the time profile of LEMMS and MAG measurements. The date of the event is shown above the panels. Starting from the top, plotted are differential intensities (counts/(cm² sr s keV)) from electron channels E0–E4 and E6, followed by energetic proton intensities (channels A0–A7, P2). Energy passband information is given at the bottom-right of each figure. Time series of the magnetic field components in spherical coordinates are shown in panels 3–5. The radial component is positive outward from Saturn, the theta component is positive southward, and the azimuthal (phi) component is positive in the direction of corotation. Blue and green curves show predictions from the K06 model for two values of the solar wind dynamic pressure. The lowest panel has the local pitch angle (α_i) for the electrons E-channels. The corresponding local pitch angle for the ion channels A0–A7 (2nd panel) is $180^\circ - \alpha_i$, excluding channel P2 which has the same pointing as the electron E-channels. In order to provide some context, the time interval plotted includes approximately 3 h of data before and after each identified pulsed event (if data are available).

Two additional subpanels are shown on the top right of Fig. 1. They mark the location of Cassini during the pulsed event (blue crosses), overplotted along its orbit (green line). The plotted

trajectory corresponds to a period of half an orbit before and after the pulsed event for which LEMMS and MAG data are available. The coordinate system used is the Saturn Equatorial System (SZS). The primary z-axis is parallel to the spin axis of the planet. The y-axis is defined as the cross product of this vector with the Saturn–Sun vector (points to dusk). The x-axis completes the right-handed system, and is on the planetary equatorial plane, directed towards the Sun. The top panel is for the orbit projected on Saturn's equatorial plane (xy), while the lower panel shows the north–south xz projection. The intersection of the magnetopause surface with the xy and xz planes is also drawn for two cases of solar wind dynamic pressure ($2 \cdot 10^{-3}$ and $4 \cdot 10^{-2}$ nPa) and, based on the Kanani et al. (2010) model. A red arrow in the xz-panel indicates the direction to the Sun, which changes with time.

3.1.1. Example 1: days 108–109/2006

We now focus on the specifics of Fig. 1 event, observed on days 108 and 109 of 2006. Cassini was crossing a region close to the magnetopause and in a local time sector where the Voyager-2 observations took place (Schardt et al., 1985), but at more equatorial latitudes. Two sets of pulsed events are seen in the top panel, the signal of each extending up to channel E4. The total duration is between 7 and 8 h, with sawtooth peaks appearing approximately every 60 min. Ion observations (2nd panel) are mostly at background, except for a short time ~ 6 h after the beginning of the plotted interval, where an enhancement in channel A1 is visible. Some ion data of channel A0 are removed for periods when there was light contamination. The magnetic field vector experiences some rotations, but with no obvious correlation to the electron features, excluding maybe hours 3–6 (as evidenced in the variation of the LEMMS pitch angle, determined by field vector rotations in this example). The LEMMS pointing is around 90° pitch angle for most of the time.

3.1.2. Example 2: day 325/2006

The second example is shown in Fig. 2. The clear quasi-periodic electron signature was recorded on day 325 of 2006, during a north, high-latitude crossing (40 – 50°) of the pre-dusk magnetosphere. The injection was at a very similar location and has nearly identical electron signatures as the ones reported by Mitchell et al. (2009) from day 269 of 2006. One significant difference is that the azimuthal magnetic field component (B_ϕ) in Fig. 2 shows a continuous perturbation, while in Mitchell et al. (2009) B_ϕ (field-aligned current) signatures were quasi-periodic and coincident with the rise times of the electron pulses. Intensities of energetic ions show some variations but it is unclear if that signature is associated with the electron event. The high electron and ion intensities at the beginning of the interval are from Saturn's radiation belts. The pulsed event appears adjacent to this trapping region. Application of the K06 field model for different solar wind dynamic pressure indicates that Cassini is most likely on closed field lines, mapping to equatorial distances between 40 and 50 R_S at dusk. Particle observations are at a pitch angle of 90° , meaning that these electrons are mirroring locally.

3.1.3. Example 3: day 291/2008

Fig. 3 includes observations from an orbital segment of Cassini across Saturn's high-latitude ($\sim -70^\circ$), southern magnetosphere on day 291 of 2008, few hours after the crossing of the Saturn Kilometric Radiation (SKR) generation region (Lamy et al., 2010). Cassini was moving outbound and at local times between dawn and noon. One particular aspect of this event are the very high intensities of energetic electrons at all energies. For instance, energetic electron intensities measured by channels E0–E3 are

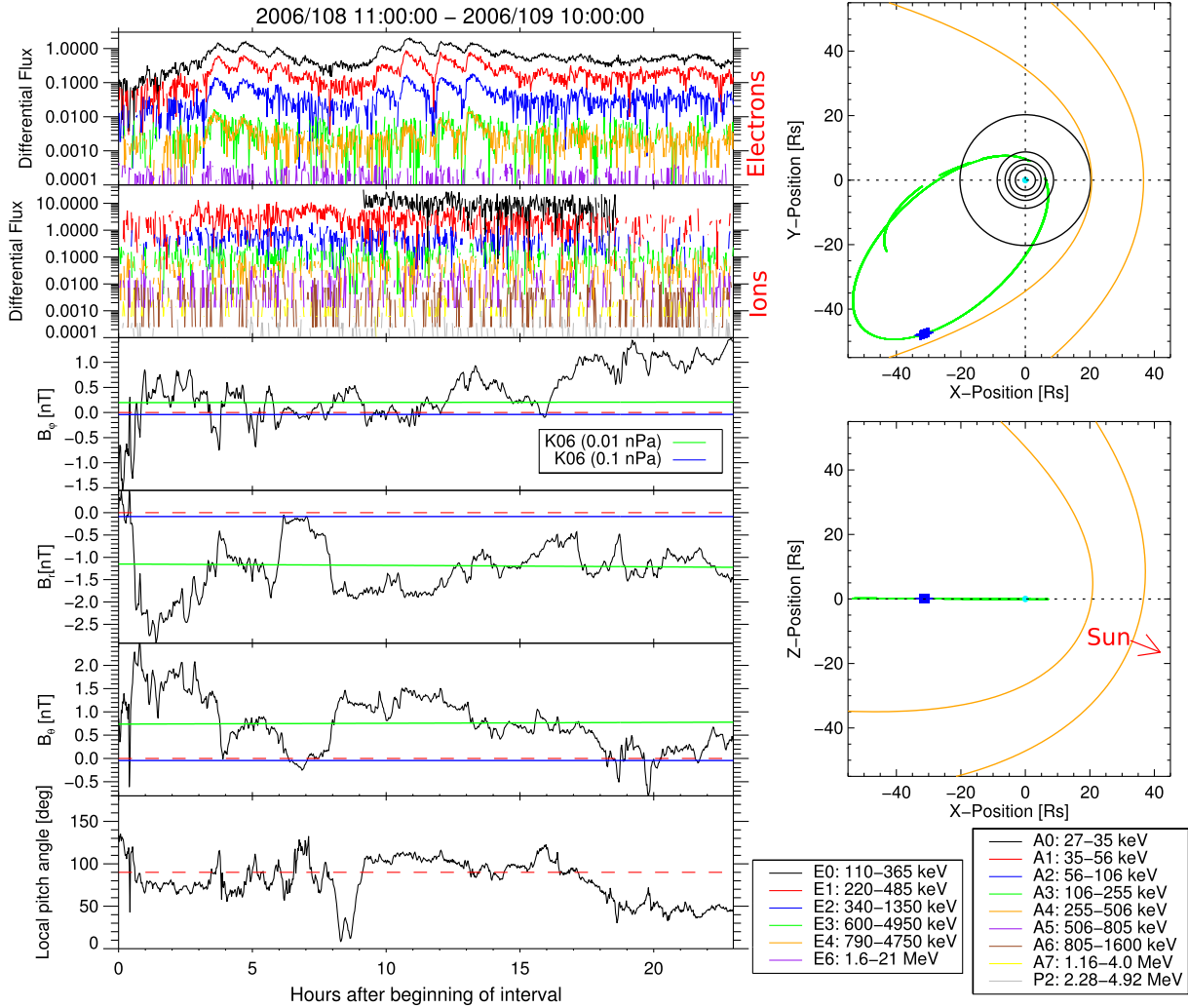


Fig. 1. Electron pulsed event from days 108–109/2006. The left panels from the top show time series of energetic electron and ion intensities (counts/(cm² s sr keV)), the magnetic field components by MAG in spherical coordinates (B_ϕ , B_θ , B_z) and the local pitch angle of the LEMMS High Energy Telescope (α_l). The time range of the event is indicated on top of the panel stack. Time in the x-axis is calculated in hours since the beginning of the plotted interval. Blue and green curves on the MAG panels show predictions from the K06 magnetic field model for two values of the solar wind dynamic pressure. Red dashed lines in the magnetic field and the local pitch angle panels mark the zero nT and 90° pitch angle values, respectively. Additional panels and legends on the right indicate Cassini's position along its orbit (green), during the pulsed event observation (blue crosses), and the energy passbands of the electron and proton channels of LEMMS. Solid circles in the panel with the equatorial (xy) orbit projection mark several saturnian moon orbits for reference (from outside: Titan, Rhea, Dione, Tethys, Enceladus). More details on the figure's structure and content are given in Sections 3.1 and 3.1.1. (For interpretation of the references to color in this figure legend, the reader is referred to the web version of this article.)

comparable or higher to those typically measured in the radiation belts (Fig. 2). Furthermore, the signal is very strong in channel E6, which measures electrons above 1.6 MeV. Its energy response is broad, meaning that higher energies above this threshold are also contributing. Energetic proton channels measure foreground up to about 1 MeV, but with no specific structure. The magnetic field has a strong field aligned current signature in B_ϕ and notable disturbances both in B_r and B_θ . This region maps to closed field lines if high solar wind dynamic pressures are used. This assumption is consistent with the results of Bunce et al. (2010) who reviewed plasma, wave and MAG data from the same time period, suggesting that the magnetosphere was in a considerably compressed state. Indeed, we also note that increasing the solar wind dynamic pressure input in the K06 model even above the 0.1 nPa level improves the agreement of the simulated B_θ with the MAG observations.

3.1.4. Example 4: days 127–128/2014

In Fig. 4 we present data from days 127 to 128 of 2013, when Cassini was at intermediate, south latitudes in the post-noon

sector. LEMMS data show a quasi-periodic varying electron spectrum, with at least five or six pulses. Compared to observations presented in the previous examples, the shape of each pulse is smooth, with comparable rise and decay times. Energetic ion intensities are at the instrumental background while MAG data show no quasi-periodic feature. A particular aspect of this event is that a shorter periodicity (~ 15 – 20 min) appears superimposed on each pulse. This observation occurred during one of the 2013 auroral campaign observational blocks, during which UV and infrared observations of the aurora were acquired by Cassini. As it will be shown in follow-up sections, these in-situ observations appear to be closely linked with statistical properties of the aurora, which is why analysis of simultaneous observations from such intervals may be important for future studies.

3.1.5. Example 6: day 184/2007

The last example is from day 184 of 2007. Cassini was on an equatorial orbit at about 40 R_s from Saturn and at a local time of 15:00. At the beginning of the interval the spacecraft is in the

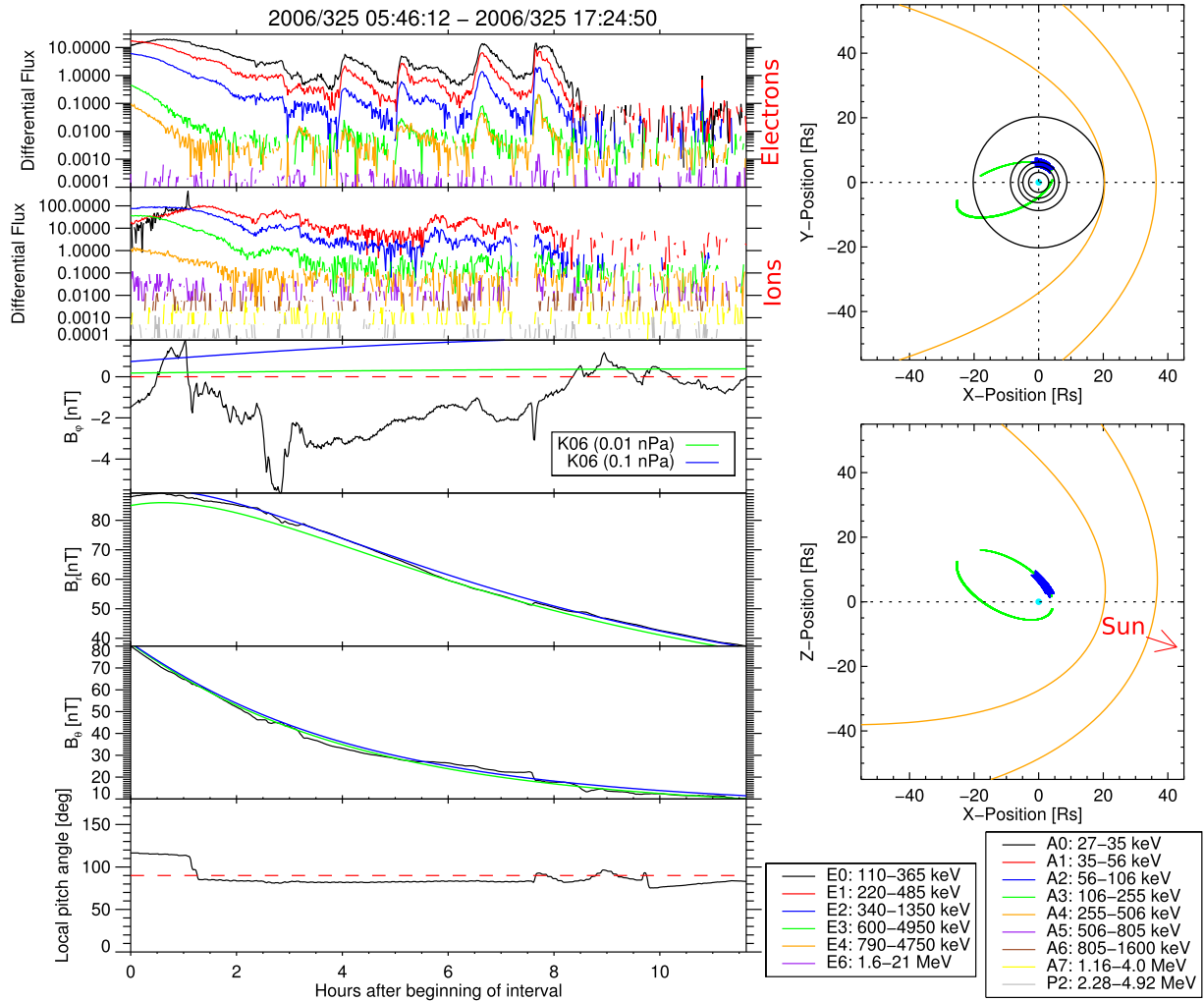


Fig. 2. Electron pulsed event from day 325 of 2006. The panel structure is identical to that of Fig. 1. More details on the figure's content are given in Section 3.1.2.

magnetosheath. Sharp changes in the magnetic field vector components mark the transition across the magnetopause and in the magnetosphere, where LEMMS observes 4 pulses of energetic electron intensity, separated by about 1 h. This signal is interrupted as Cassini enters for an extended period once more into the magnetosheath. While in previous examples the proximity of the pulsed events to the magnetopause was based on empirical models of its location, this example shows directly that these features can actually extend up to the magnetopause. The origin of the enhanced electron intensities may also be connected to dynamics along this magnetospheric boundary. The event is also tightly confined within the two boundary crossings, with no indications of electron leakage into the sheath.

3.2. Survey

The presentation of the five examples in Section 3.1 demonstrates that the most common characteristic is the repetition of the electron enhancements every about once an hour. When we factor in additional examples, not shown here, and perform an initial frequency analysis for a sample of those, we find that the inter-pulse period distribution peaks between 60 and 70 min. For simplicity, we will refer to the events from this point onwards as “QP60” (“QP” stands for “quasi-periodic”), which is representative of the discussed events, even if follow-up studies may refine the mean period value few minutes away from the single-hour range.

The naming is based on the quasi-periodic properties of events with more than two pulses. The use of “quasi-periodic” may not be fully appropriate for cases that only two pulses have been detected. The reason that we adopt this term also for cases with two pulses is due to the morphological similarities of these events (shape of pulses, interpulse period) with the longer-duration examples, which indicates that they are, without doubt, the same type of phenomena. The fact that the interpulse period is always around 60–70 min means that QP60 are temporal features. If these structures were spatially organized, the interpulse duration would have varied from event to event, depending on their crossing geometry by Cassini.

The survey for QP60 was driven by the detection of the quasi-periodic signal in the energetic electron spectrum. It was performed using manual inspection of various types of standard, daily time series plots of LEMMS data. In order to include an interval in our list of events we assigned several criteria:

1. Only LEMMS electron data should be used for the selection, since coincident magnetic field or energetic ion observations, even on very similar pulsed electron events, had varying responses. Magnetic field data should at least be available for the calculation of particle pitch angles.
2. The injections should include at least two pulses, with a time separation (or period, in case of many pulses) in the range of 40–80 min. The sawtooth shape (rapid rise, slow decay) was

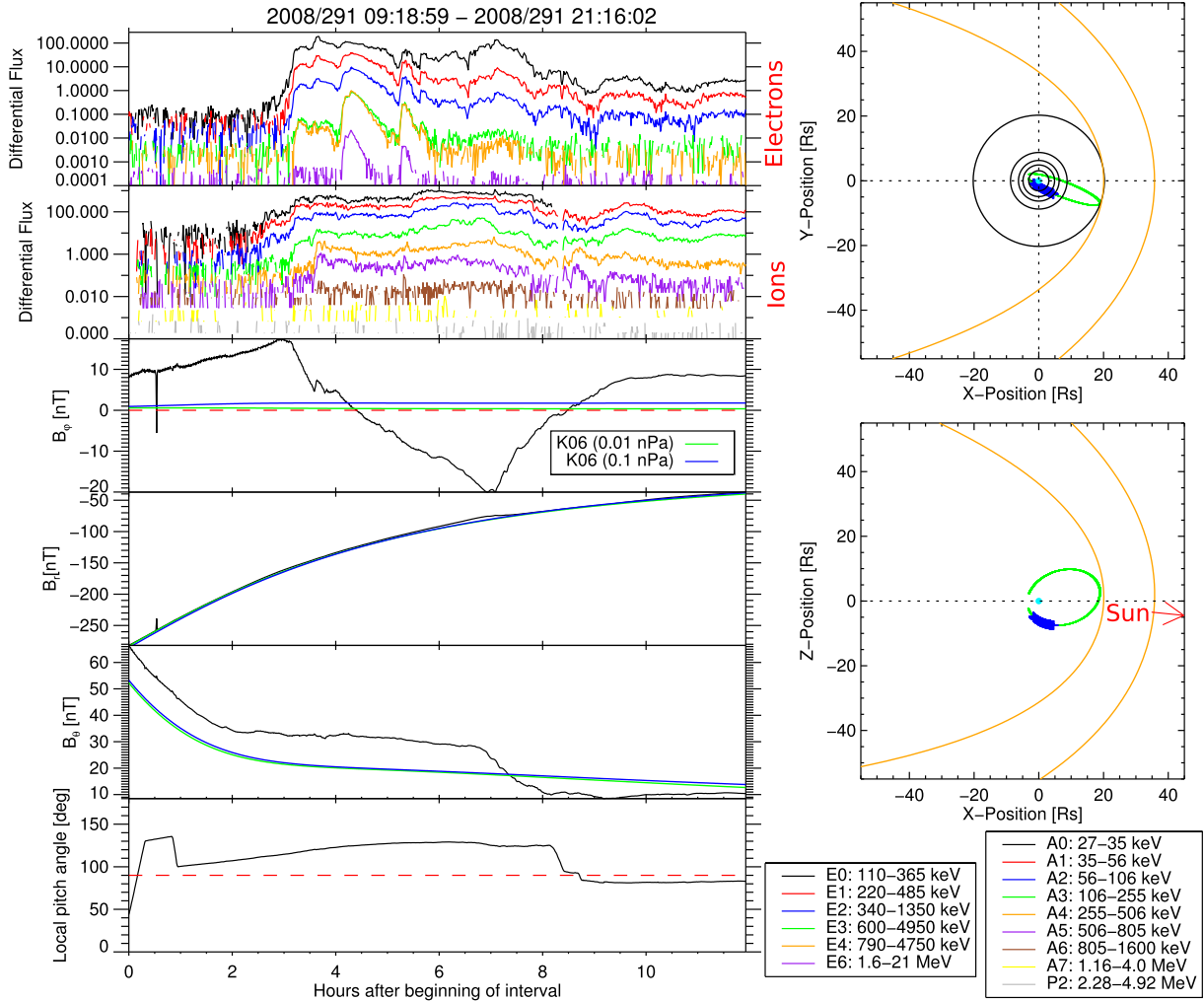


Fig. 3. Electron pulsed event from day 291 of 2008. The panel structure is identical to that of Fig. 1. More details on the figure's content are given in Section 3.1.3. This time period has also been reviewed in Bunce et al. (2010).

not required for the selection, as this would have excluded cases like those of Examples 4 or 6. Separation of the events according to the rise time of the pulse can be later applied to all the resulting dataset.

3. The signal of such an event should appear at least in one of the E0–E7 channels of LEMMS (>95 keV). Relatively few events were visible below 95 keV, so we restricted our search using only LEMMS's E-channels. Furthermore, any event that appeared below 95 keV had in all cases a signature also above 95 keV. We note here that the lack of detection below about 95 keV is not because of a low-energy cutoff for the QP60, but because the signal of the pulses mixes up with other electron populations and can be difficult to distinguish. This is demonstrated later (Section 3.3.1).

For validation purposes, we repeated our survey eight times. Some of the aforementioned criteria were slightly varied for several of those surveys. For instance, setting the minimum energy to 50 keV or to 200 keV had a small impact on the spatial distribution of the QP60 (discussed later) or even the size of our statistical sample. The final list that we use here consists of 543 time QP60 intervals. This number varied by less than 7% between different surveys performed and had no impact on our statistical results. 68 cases had an electron spectrum with foreground in channel E6 (1.6–21 MeV).

In order to reduce the effects of possible selection bias, we also applied a wavelet analysis on the LEMMS channel time series. Results of wavelet analysis, on the other hand, had to be carefully interpreted since spacecraft rolls with periods close to the 40–80 min range could introduce similar periodicities in the data. Data gaps could also cause misleading artifacts in a wavelet spectrum, which also explains why automatic algorithms were avoided for the survey. Other frequency analysis methods, such as the Lomb–Scargle analysis, are more useful if the start and stop times of each event are known (e.g. for measuring the period of each QP60), so they were less appropriate for surveying the LEMMS dataset.

None of the QP60 triggered a response in electron channel E7 (>7 MeV). This is likely due to the relatively small geometric factor of this channel, rather than an upper limit in the energization of electrons, as discussed in Section 3.3.2.

3.2.1. Spatial distribution

We first focus on the injections observed at low latitudes (Fig. 6): we keep data within $2 R_s$ from the equatorial plane of Saturn since the current sheet is usually located within this range (Arridge et al., 2008).

In Fig. 6 we plot the orbit of Cassini (green dots). Blue crosses along the trajectory indicate the locations of QP60 events. Yellow circles mark the cases that also have a foreground signal in

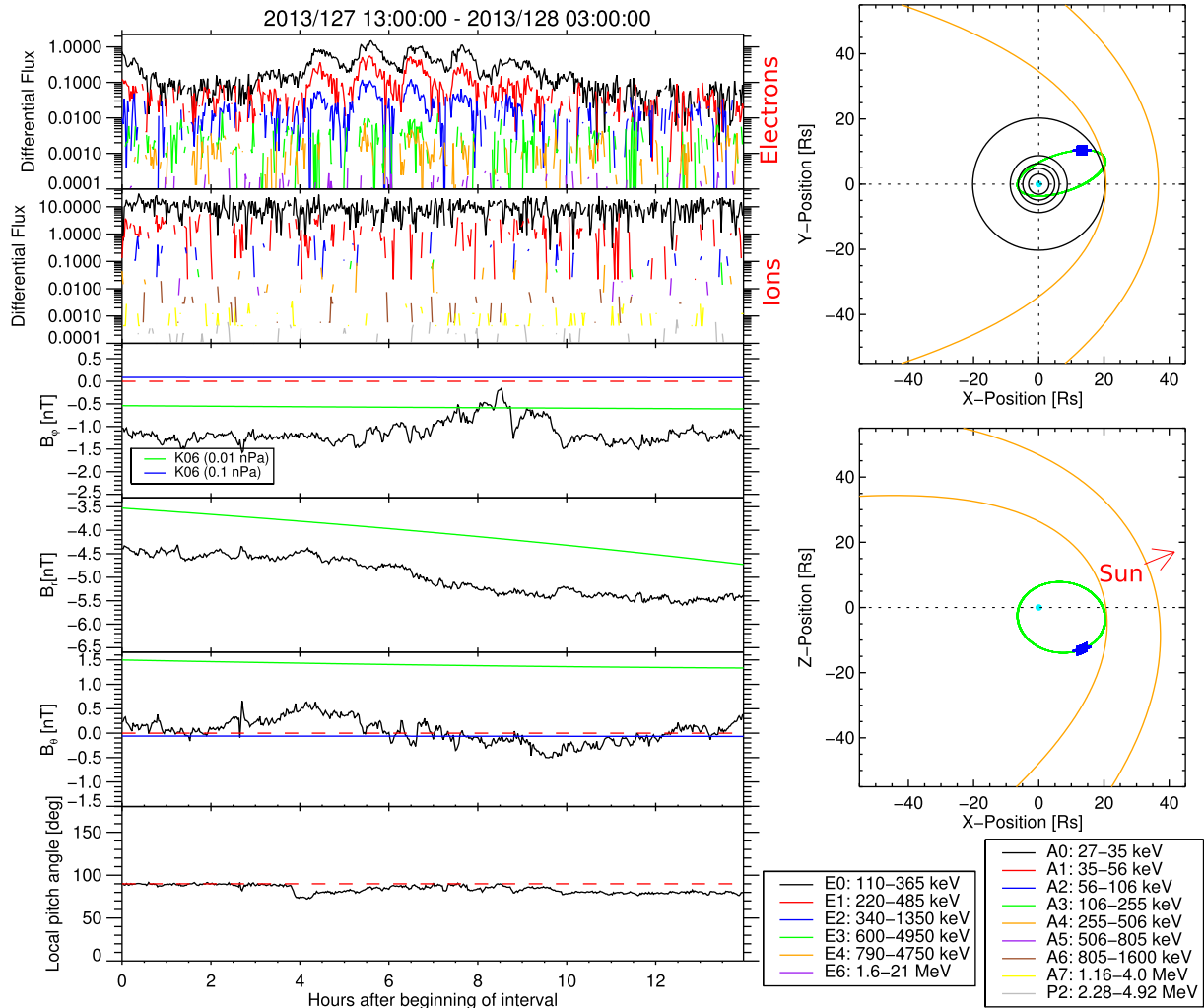


Fig. 4. Electron pulsed event from days 127 and 128 of 2013. The panel structure is identical to that of Fig. 1. More details on the figure's content are given in Section 3.1.4.

LEMMS channel E6 (1.6–21 MeV). The magnetopause is drawn for different values of the solar wind dynamic pressure. The outermost magnetopause curve is for a pressure of 10^{-3} nPa and for every subsequent curve the corresponding pressure value is doubled.

The data indicate that QP60 may be observed at all local times, but this distribution is clearly asymmetric: many more are encountered around dusk, although all local times are covered by Cassini. The majority of the injections are observed outside Titan's orbit. The only two exceptions are from days 182 of 2006 (Cassini moving outbound, from dusk to midnight) and 225 of 2011 (Cassini moving inbound at dusk), where QP60 was seen down to 12 and 16 R_S , respectively.

The largest concentration of QP60 is found post-dusk. Many were also encountered relatively deep inside the predicted locations of the magnetopause. The highest energies (yellow circles) are also observed in the post-dusk sector, but are also fairly common in local times between 15:00 and 18:00. A foreground signal in channel E6 is a good indicator for the most intense electron spectra (Fig. 7): the largest, average intensities of the E0 channel (110–365 keV) are also at the location where the majority of E6 electron detections occur.

The latitudinal distribution is shown in Fig. 8. The format is similar to Fig. 6, but data are projected in local time–latitude space. All points map to the outer magnetosphere, so distance information is secondary for this plot. The most important aspect is that QP60 extend also towards dawn, with many high intensity/energy

events (yellow circles) in the southern, high-latitude magnetosphere. The absence of corresponding signatures at the dawn, equatorial magnetosphere could mean that these events map to open field lines allowing electrons to escape the system before reaching low latitudes. Alternatively, if they are on closed field lines (see discussion for “Example 3”, Section 3.1.3), the corresponding equatorial traces may be at large distances or in a confined region that has not been sampled by Cassini (see also Section 3.2.2). The lack of events at the northern, dawn hemisphere could be due to the low sampling of the respective latitudinal range above 50° .

When the number of QP60 detections is normalized to Cassini's residence time in the various local time sectors, the dawn–dusk asymmetry remains (Fig. 9). This indicates that the asymmetry visible in Figs. 6 and 8 is not due to sampling issues. The frequency of QP60 occurrence is almost a factor of 10 higher at the duskside where QP60 are observed every about 4–6 days, as opposed to 1 event over 20–100 days at the dawn magnetosphere.

3.2.2. Magnetic mapping

We now trace those distributions on two reference surfaces using the K06 magnetic field model. The first is the equatorial xy-plane and the second is the planetary ionosphere. In both cases the K06 model is used for two values of the solar wind dynamic pressure (0.005 and 0.05 nPa). Since the dynamic pressure

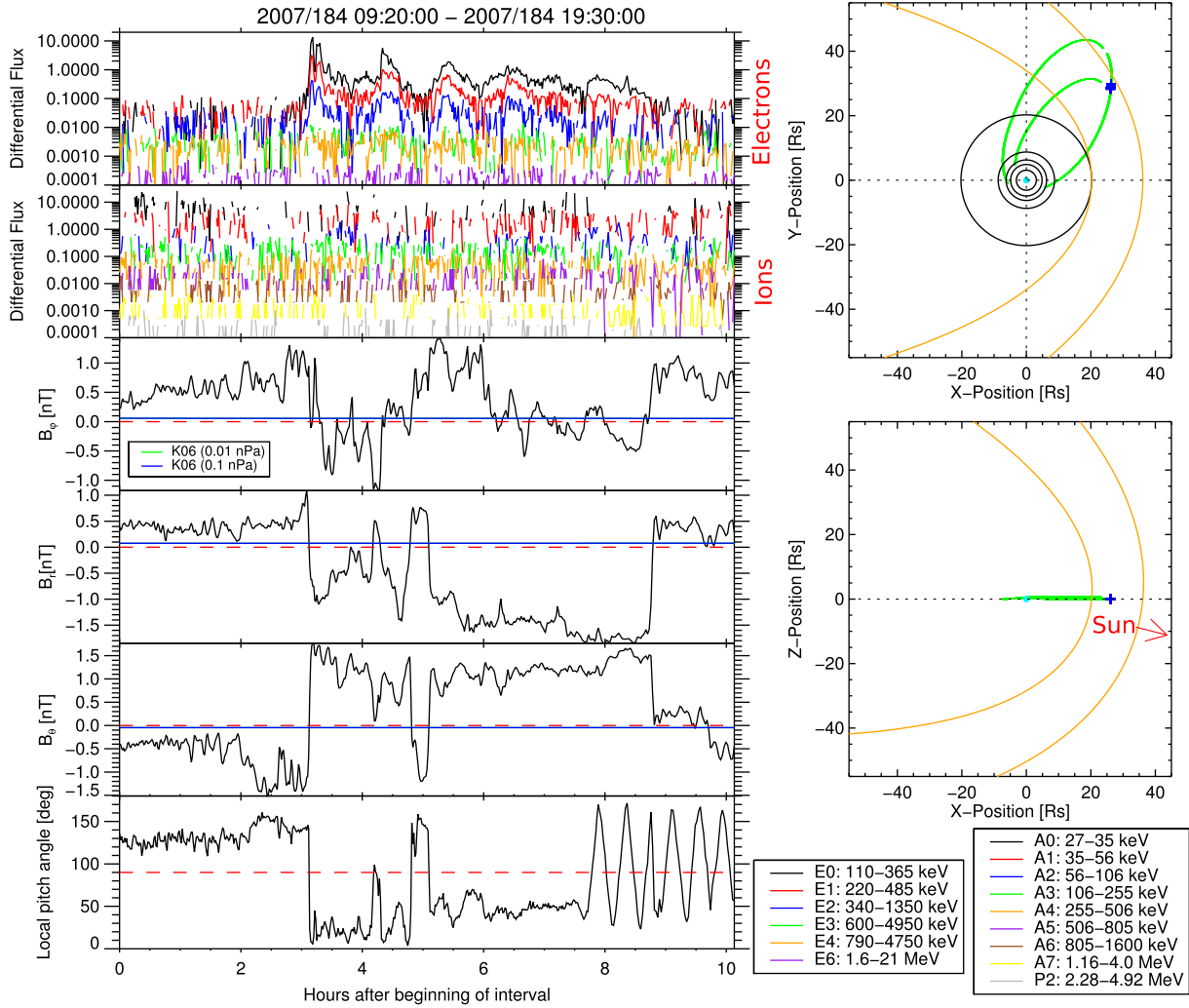


Fig. 5. Electron pulsed event from day 184 of 2007. The panel structure is identical to that of Fig. 1. More details on the figure's content are given in Section 3.1.5.

“calibration” of the K06 model is only approximate, we refer to the two cases as low and high pressure cases, respectively.

The four panels of Fig. 10 show the equatorial mapping of the QP60 locations. The different rows are for the low and high dynamic pressure mapping, while the right column includes only the MeV event traces. Blue points are for cases where Cassini was within $2 R_S$ from the equatorial plane of Saturn. Red points correspond to all other, higher latitude events.

Due to the K06 model uncertainties for the outer magnetosphere, the exact coordinates of the final traced locations from off-equatorial events are likely highly inaccurate, especially if the resulting point is beyond a distance of $30 R_S$ in the magnetotail or $\sim 40\text{--}50 R_S$ at other local times. For that reason we focus on the qualitative/statistical similarities of the low and high pressure maps (panels “A” and “C”). Those signify characteristics that are less dependent on the field model accuracy.

The tracings verify that the majority of the events, including the high-latitude ones, map to beyond the orbit of Titan. Both high and low pressure scenarios indicate that the region between about 15:00 local time and midnight (moving anticlockwise) is highly dynamic, with most QP60 mapping mostly post-dusk at around 20:00–21:00 local time. In both configurations the center of this post-dusk region is situated well inside the magnetopause. For local times between noon and dusk, the result depends on which pressure case is used, so we cannot be certain: for high pressure,

QP60 concentrate at the magnetopause boundary while for low pressure many of them still map several R_S inwards. We note, however, that in the high-pressure case about 35% of QP60 observations are absent from panel “C”, as they were situated outside the K06 model magnetopause and therefore field line tracing was not possible. The results described above are similar also for the MeV events (panels “B” and “D”).

We now move to the local time sector between about 3:00 and 12:00. Data in panels “A” and “C” indicate that most QP60 map along the magnetopause boundary. The additional cases that are visible in panel “C” but not in panel “A” appear because they map to closed field lines of the K06 model only for the high pressure field configuration. Only a small fraction of the MeV events (panels “B” and “D”) have an equatorial trace in this local time range, as a large number is on open field lines of the K06 model (see also Fig. 11). Also here the MeV events appear to trace to the magnetopause.

Fig. 11 shows the results from the mapping of the QP60 to the north and south planetary ionosphere. Similar to Fig. 10, rows separate low from high dynamic pressure tracings. The left(right) column is for the northern(southern) hemisphere. Blue circles mark conjugate QP60 events, which are those that are on closed field lines and can be therefore be traced to both the northern and the southern ionosphere. Red points mark QP60 on open field lines, meaning those that have a trace only on one of the two

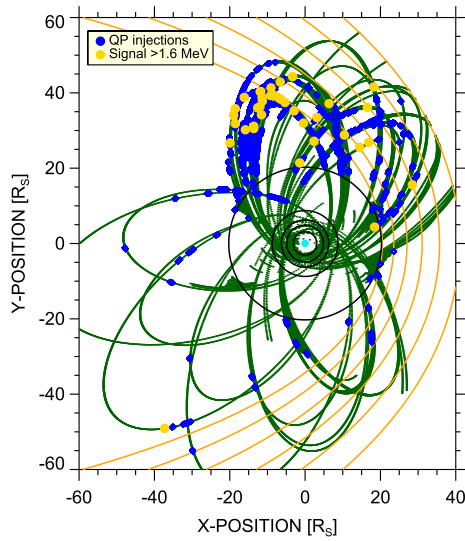


Fig. 6. QP60 event locations (blue points) along the Cassini trajectory within $2 R_s$ from the equatorial plane of Saturn. Yellow circles mark the events with high intensity/energy, based on the detection of foreground signal in LEMMS channel E6 (1.6–21 MeV). The outermost magnetopause curve is for a pressure of 10^{-3} nPa, and for every subsequent curve the corresponding pressure value is doubled. Data and the orbit are plotted only within the boundaries of the most distant magnetopause considered here, as pulsed events were not seen beyond it. (For interpretation of the references to color in this figure legend, the reader is referred to the web version of this article.)

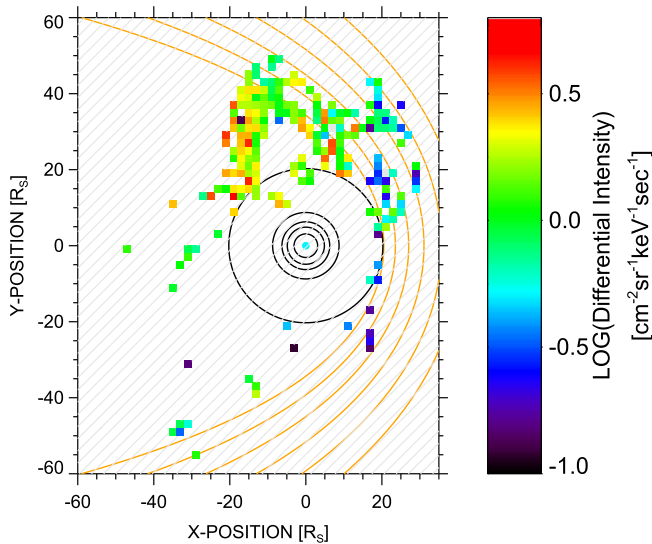


Fig. 7. Binned differential intensities of E0 channel (110–365 keV electrons) along the equatorial locations that QP 60 events have been observed. Highest intensities are seen where the most relativistic electrons are also observed (Fig. 6). Hatched areas indicate lack of data or QP60 observations.

hemispheres. Open green circles correspond to the MeV events. The magenta line is for the mean position of the main aurora emission and the black lines denote its statistical boundaries (Carbary, 2012). Mapping high latitude events to the ionosphere is more accurate than tracing them to the equator, since the high latitude region is dominated by the planet's internal field which is well defined.

One common feature in at least three of the panels (“B”, “C” and “D”) is that the distribution of QP60 on closed field lines (blue points) appears to have a poleward extension starting at a local time of about 10:00 and peaking at 15:00. These properties appear also in the average profile of the main aurora emission (magenta

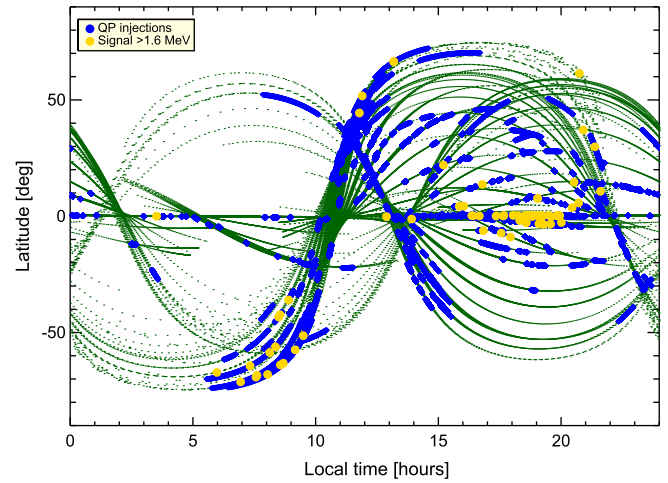


Fig. 8. QP60 locations (blue points) along the Cassini trajectory and as a function of local time and latitude. The meaning of the different data points is the same as in Fig. 6. (For interpretation of the references to color in this figure legend, the reader is referred to the web version of this article.)

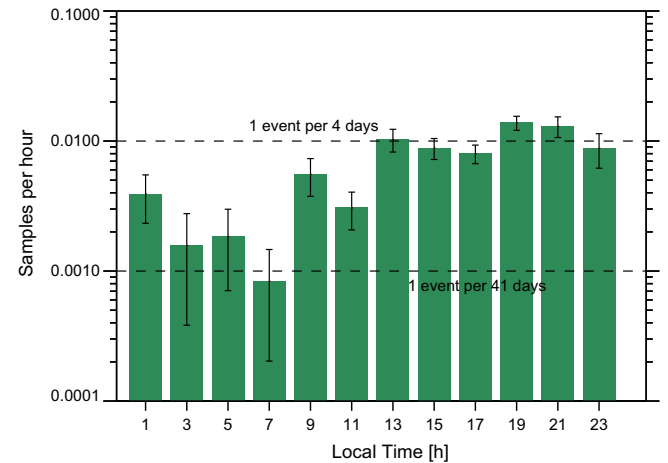


Fig. 9. Frequency of QP60 occurrence as a function of local time. The error bars are calculated from Poisson statistics on the number of events within each local time bin and are extended assuming a systematic uncertainty of 7% in the event number estimation (see Section 3.2).

line). Another characteristic is the larger number of closed field line events between 10:00 and midnight (moving anticlockwise). This coincides with a large change in the statistical width of the main emission between local times of 15–20 h. That is also the region where most MeV events are observed, both in the maps of Fig. 11 and on the equatorial ones (Figs. 6 and 10).

The statistical results described above for the local time sector of 10–24 h are similar for both hemispheres and for the different assumptions of the solar wind dynamic pressure. Where we see better evidence for hemispherical and solar wind dependencies is the local time range from midnight to about 10:00. Many QP60 have a trace only to the southern hemisphere since they are on open field lines (red points). Only few of these red points may “transit” to closed field lines if we assume a higher solar wind dynamic pressure for the K06 model (panel “D”). Overall, these QP60, which include also most of the MeV events of that local time sector, map poleward of the main aurora emission. Their source is most likely located in the southern hemisphere unless we assume extreme solar wind conditions which allows to have conjugate points in the northern hemisphere.

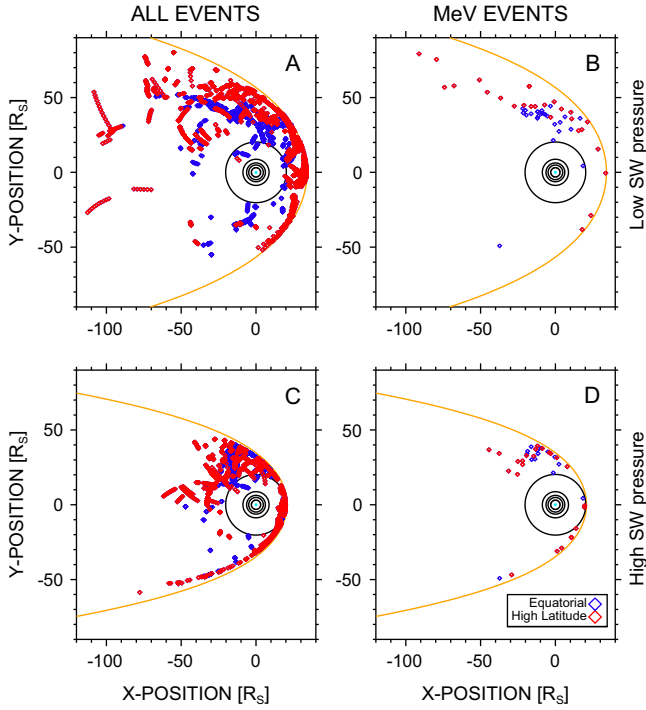


Fig. 10. Tracing of QP60 on the equatorial xy -plane using the K06 model for two different solar wind dynamic pressure values. The different rows are for the low and high dynamic pressure. The right column includes only the MeV events (>1.6 MeV). Blue points indicate the starting point of the tracing was within $2 R_S$ from the equatorial plane of Saturn (Fig. 6). Red points correspond to all other, higher latitude events. (For interpretation of the references to color in this figure legend, the reader is referred to the web version of this article.)

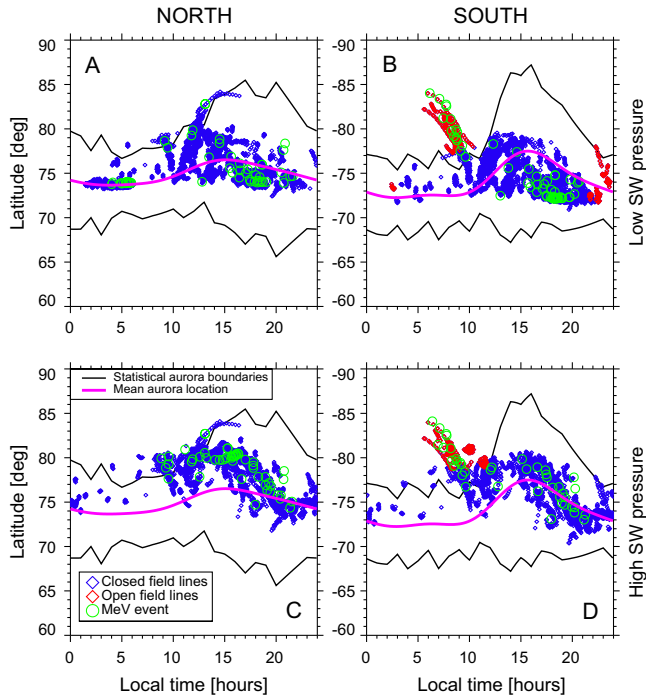


Fig. 11. QP60 locations mapped to the north and south planetary ionosphere. The left (right) column is for the northern (southern) hemisphere. Blue points mark events on closed field lines, red points are for QP60 on open field lines. Open green circles indicate the MeV events (>1.6 MeV). The magenta line is for the mean position of the main aurora emission. Black lines denote the main emission's statistical boundaries (Carbary, 2012). (For interpretation of the references to color in this figure legend, the reader is referred to the web version of this article.)

3.3. Additional aspects

In Section 3.2 we focused on the topology of the QP60. Here we only highlight some additional, important aspects, but a more detailed statistical analysis of those features will be analyzed in detail in future works.

3.3.1. Pitch angle distributions

As stated in Section 2, pitch angle distributions are frequently not available, as Cassini needs to perform a roll while LEMMS is sampling a QP60. The available cases, however, offer a good opportunity to separate different electron populations and to put in context some of the earlier results presented in Section 3.2.2. For instance, Saur et al. (2006) analyzed field aligned, energetic electron beams that, similar to QP60, were detected in the outer magnetosphere and in regions mapping to Saturn's aurora. One question is whether these beams and QP60 correspond to the same process.

For an initial approach to this problem, we discuss LEMMS observations from day 48 of 2009, during which LEMMS sampled all pitch angles. Fig. 12 shows LEMMS time series from the event (top panel) together with the pitch angle pointing of the LEMMS HET (bottom panel). Low energy electron channels (C0, C2, C5,

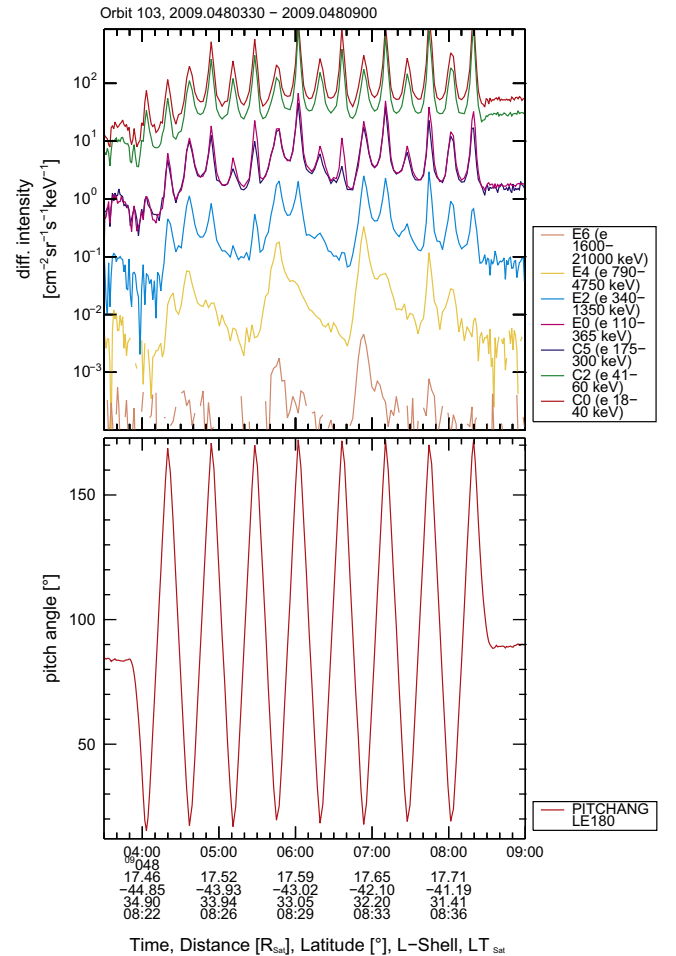


Fig. 12. Time series of a QP60 from day 48 of 2009 in various LEMMS electron channels (top panel) together with the pitch angle pointing of the LEMMS HET (bottom panel). Position information for Cassini is also provided in the time axis. Cassini was at high, southern latitudes and more than $10 R_S$ inside the magnetopause, but near the open-closed field line boundary.

E0) show a periodic variation in phase with the changes of LEMMS's pitch angle, always peaking always in the field aligned direction. The peaks are narrow and symmetric in pitch angle (C5/E0 ratio is one), indicating a bidirectional beam structure that resides on closed field lines, similar to what is reported by Saur et al. (2006). The conclusion about Cassini being on closed field lines follows from the method in Gurnett et al. (2010): since LEMMS channels C5 and E0 sample approximately the same electron energies but look on opposite directions, their differential intensity ratio should be close to unity while LEMMS points along the field and if Cassini is on closed field lines.

At higher energies (channels E4, E6) we see the typical signature of a QP60, while channel E2 appears to contain a mix of the beam and QP60 populations. The signature of pitch angle variability is much weaker in the intensity of E4 and E6, but whether temporal or pitch angle changes dominate the signal variations of these two channels is unclear. To separate temporal from pitch angle effects, we made a simple analysis of the second pulse observed with E4 (Fig. 13).

The top panel shows the pulse signal (black line) as a function of time, with $t = 0$ corresponding to the QP60 peak. The LEMMS pitch angle is plotted with the blue curve. In the first model (green line), we assume that the exponential decay of the pulse is fast and shadows changes in the flux due to a variation in the detector pitch angle. We therefore fit a simple exponential profile $j(t) = j_0 e^{-(t/\tau)}$ where j_0 and τ are fit parameters, with j_0 close to the intensity at $t = 0$, and τ the e-folding time. For this first case, only the first 500 s of data are used to make the fit, as that is the interval where the drop appears to be exponential. In the second model, we assume that time variability is dominated by pitch angle changes. In order to fit that data we should have observations at the same pitch angle. If we are on closed field lines (as we know we are) we can also use conjugate pitch angles since on closed configurations, a bounce-averaged distribution is symmetric. The best case of conjugate pitch angles for

which data are available in this interval are at 20 and 160°.

We then used the results of the fits to extrapolate each of the data points to the time of the pulse peak ($t = 0$). Results are plotted in the bottom panel of Fig. 13. We believe the red profile is more realistic, as its e-folding time (~ 500 s) compares better with that obtained from pulses that are observed at fixed pitch angle. Nevertheless, in both cases the pitch angle distribution peaks in the field aligned direction, but the overall shape is shallow rather than beam-like. Intensities are considerable also at 90° as many QP60 examples indicate (Section 3.1). We should stress, however, that the PAD of a pulse's rise time and of its decay (shown here) may have different shape, but this morphological aspect is a subject for a follow-up study. One problem is that the rise-time of pulses is very short, so PADs cannot be easily obtained.

Examples like the one of Fig. 13 are not uncommon. Similar LEMMS observations occur on days 39/2010, 269/2010, 36/2011, 208/2011 and 87/2013. The list is much longer, limited mostly by the pitch angle coverage of LEMMS. What changes between the different examples is the energy range where the two different populations can be clearly separated. Typically, the field aligned electron beams do not extend above 500 keV. On the contrary, the signal QP60 can sometimes be seen at the lowest energy electron channel of LEMMS (C0: 18–40 keV, e.g. day 36/2011).

Overall, while both energetic electron populations appear to be observed together when LEMMS obtains pitch angle distributions of QP60, their origins are possibly connected to a different process.

3.3.2. Energy spectra

In order to understand the energy range up to which electrons are accelerated and compare the differential intensities and phase space densities with those of the radiation belt seed electron population, we present here the energy spectra for the full energy range covered by LEMMS.

For all previous plots, differential intensities of the LEMMS channels were calculated using the standard equation:

$$I = \frac{C}{G\Delta E}, \quad (1)$$

where C is the count rate (in Hz), ΔE is the channel's nominal pass-band (in keV) and G its geometric factor (in $\text{cm}^2 \text{sr}$). Eq. (1) is sufficient for channels with small $\Delta E/E$ (LEMMS C and PHA channels). For the E-channels, which have a large $\Delta E/E$, the equation is sufficient if only a rough order of magnitude estimation of the intensities is required (e.g. for time series plots).

Since here we want to calculate the mean electron energy measured by channels like E4, E6 and E7 we assume a shape for the differential intensity spectrum that we constrain from observations of the lower energy PHA and C-channels ($I = I(E)$) and then apply this spectral shape in Eq. (2) for each of the three E-channels:

$$R_i = \int_{E_{\min}}^{E_{\max}} I(E) G_i(E) dE, \quad (2)$$

Here, R_i is the predicted count rate and $G_i(E)$ is the response function of each channel within the energy range E_{\min} and E_{\max} . We then require that application of $I = I(E)$ to Eq. (2) reconstructs the actual count rate of E4 and E6 within a factor of 2, while the prediction for channel E7 (which never measured foreground during a QP60) should not be more than twice its background count rate. The factor of two is used to account for uncertainties in the simulated response functions of LEMMS's E-channels and to the $I = I(E)$ profile obtained from fits to lower energy channels. After the fit parameters are obtained, we estimate the mean electron energy in each channel from Eq. (3):

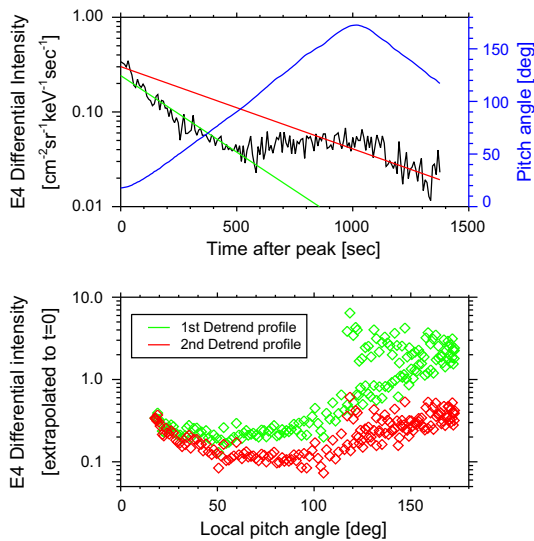


Fig. 13. (Top): Time series of E4 channel intensity for a single pulse of the day 48/2009 QP60 event. $t = 0$ corresponds to the QP60 peak. The LEMMS pitch angle is plotted with the blue curve. Two theoretical profiles were also fit to the data assuming either that the time variation of the signal is dominated by the exponential decay of the pulse (green) or that the pitch angle variation is more important (red). (Bottom): The pitch angle distribution (PAD) of the pulse at $t = 0$, as it results from the different pulse detrending profiles. (For interpretation of the references to color in this figure legend, the reader is referred to the web version of this article.)

$$E_m = \frac{\int_{E_{\min}}^{E_{\max}} I(E) R_i(E) E dE}{\int_{E_{\min}}^{E_{\max}} I(E) R_i(E) dE}, \quad (3)$$

and the corresponding intensity by $I_m = I(E_m)$.

The choice of $I = I(E)$ is not unique, and we attempted fits with simple power-law functions, kappa-distributions, spectral forms described in Aguilar et al. (2013) or combination of those. In all cases, the spectrum above several hundred keV could be well represented by a single power-law distribution.

Fig. 14 shows the results for two examples of intense QP60, one at high latitudes (day 291/2008 – Example 3, Section 3.1.3) and one at equatorial latitudes, a magnetospheric local time of 19:30 and a distance of 42 R_S from the planet. The energy spectrum (top panel) has a power-law shape beyond about 100–200 keV with no obvious spectral breaks. The few points from PHA-channels which could indicate a steeper power-law beyond 1 MeV are likely due to the low sensitivity of the respective channels in that range (as seen also by the larger error bars). Assuming such a steep spectrum will not reconstruct the count rates of E4 and E6 channels. The mean energy for channel E6 in this plot (rightmost points) is between 4.5–6.0 MeV. We also expect that the spectrum extends at least up to 10 MeV, but the geometric factor of E7 is too low to detect the signal.

The bottom panel of Fig. 14 shows the same data converted into phase space density and plotted as a function of the first adiabatic invariant (μ). The profiles are also compared with that of the ring current based on the analysis of Kollmann et al. (2011), in order to evaluate whether QP60 can be a potential source for the ring current (Section 4.3). Phase space densities of QP60s at any given value of μ are between three and four orders of magnitude above those at the ring current.

Following the method of Thorne (1983) and taking that 1 mW/m² of precipitating intensity corresponds to 10 kR emitted UV intensity at the ionosphere (Grodent et al., 2001), we estimate (using the spectra of Fig. 14) a contribution to the aurora brightness of about 0.19 kR.

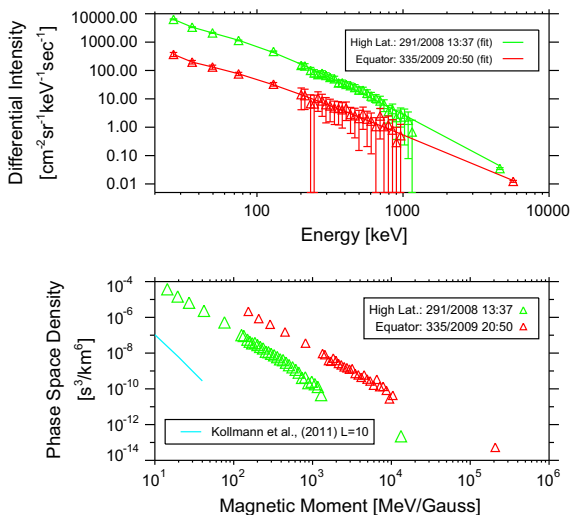


Fig. 14. (Top): Energy spectra for two intense QP60, one at high latitudes (green points, day 291/2008, Example 3, Section 3.1.3) and one at equatorial latitudes from day 335 of 2009, at the post-dusk sector. The five lowest energy points are from rate channels C0–C5, the intermediate energies are from the PHA-F channels and the highest energy point is from rate channel E6. PHA-F channel measurements above 1 MeV were not considered due to their low sensitivity. The 2009 event was at a pitch angle of 170°. (Bottom): The same spectrum, converted into phase space density and plotted as a function of the first adiabatic invariant (μ). (For interpretation of the references to color in this figure legend, the reader is referred to the web version of this article.)

4. Discussion

In this work we presented the first statistical analysis of short period, quasi-periodic energetic electron injections, using almost nine years of energetic electron and magnetic field measurements by Cassini's MIMI/LEMMS and MAG instruments. These injections, which we label as QP60 since they most commonly repeat every about 60 min, were previously analyzed in single case studies (Schardt et al., 1985; Mitchell et al., 2009; Badman et al., 2012), which did not provide information about their topology and frequency of occurrence.

Besides their characteristic period, all of the detected QP60 appear to be dispersionless with electron energy. This may suggest that they are either short-lived or that the magnetic field gradients in the outer magnetosphere are too weak for energy-time dispersion to develop due to gradient/curvature drifts, as seen for injections in the inner magnetosphere (Mauk et al., 2005).

Magnetic field and energetic ion observations by MAG and LEMMS do not appear to have a standardized, coincident signature with the electron events. The reason behind that is not clear to us, but it is probably associated with the multiple processes that can generate a QP60, as we discuss later, and to parameters such as the observational altitude along a field line or even the age of an event which cannot yet be estimated.

With regards to energetic ions, it is also important to note that Mitchell et al. (2009) reported the presence of conics or field-aligned ion beams during a QP60, using observations from the Ion-Neutral Camera of MIMI (INCA). Zhang et al. (1995) found similar structures at the onset of quasi-periodic electron bursts at Jupiter. If indeed the energetic ion counterpart of QP60 exists only in the field-aligned direction, it is very possible that we missed the possible coincident ion signatures due to the limited pitch angle coverage by LEMMS and/or its much lower sensitivity compared to INCA. A future review of INCA observations may clarify whether ion conics are a typical feature of QP60. If so, it would point to an electron acceleration source near the ionosphere.

What we nevertheless believe is the most important observation is that QP60 are detected globally in Saturn's magnetosphere, at a wide range of local times and latitudes (Figs. 6 and 7). The only location that events appear to be uncommon is a 1–2 h wide sector centered around 03:00 local time, although this location of the magnetosphere has not been densely sampled. The majority of QP60 map outside the orbit of Titan and their local time distribution and characteristics show a strong asymmetry between dawn and dusk. Based on this asymmetry, we divide the magnetosphere in two broad sectors, roughly separated by the noon-midnight line, and organize the discussion points below accordingly.

4.1. Dusk magnetosphere

QP60 are very common in the duskside magnetosphere, extending all the way from noon to midnight (moving anticlockwise). Their signature can be detected at all latitudes visited by Cassini, consistent with our inference from field-line tracing, that QP60 on that sector reside on closed field lines.

An important aspect of the duskside QP60 is that almost all events map magnetically within the statistical auroral boundaries. Their distribution traces well the typical local time structures of the aurora (Fig. 11), such as a poleward offset of the main emission's center and its broadening between noon and 21:00 LT (Carbary, 2012). The broadening is not a steady-state structure. It reflects transient, dynamic processes in that region of the magnetosphere (Radioti et al., 2011). This is also in agreement with our inference of a very dynamic dusk magnetosphere based on the high frequency of QP60 detections and the large number of events with a detectable signal in the MeV electron channels of LEMMS.

These correlations suggest that signatures associated with QP60 may be detected in imaging sequences of the aurora. That would allow to study the response of the magnetosphere during a QP60 interval in a global scale. It is, however, not yet clear which aspects of the aurora could be the QP60 counterparts. For instance, Radioti et al. (2013) reported the observation of recurrent auroral brightenings separated by about 60 min which may map to a QP60 region. On the other hand, Mitchell et al. (2009) and Badman et al. (2012) associate QP60 with the aurorally dark, downward current regions. The low, estimated UV brightness from the QP60 electrons (<2 kR – Section 3.3.2) is more consistent with the latter interpretation.

We now split the duskside into post- and pre-dusk. A motivation for that is the detection of the highest intensity events in post-dusk (or pre-midnight) sector, with many of them clustering far from the magnetopause and across an area oriented parallel to the dawn–dusk line (y-axis, Fig. 6). The distance of the post-dusk group of QP60 from the magnetopause, implies that magnetopause-driven processes, such as reconnection and/or Kelvin–Helmholtz (KH) instability must be excluded as responsible for the QP60 origin. This argument holds unless we assume that the boundary layer at the dusk flank can be as thick as $30 R_S$. Walker et al. (2011) estimated boundary layer thicknesses of less than few R_S based on MHD simulations of Saturn’s magnetosphere. Furthermore, Delamere et al. (2013) found no evidence of KH-instability signatures deeper than few R_S from the dusk magnetopause.

A possibility to interpret post-dusk sector observations can be based on theoretical expectations for the plasma circulation in Saturn’s magnetosphere (Cowley et al., 2005) (see their Fig. 2a) and the detection of inflows and outflows by Thomsen et al. (2013) in that location. Cowley et al. (2005) predicts that closure of planetary field lines following the release of mass loaded flux tubes with heavy water-group ions, which is part of the Vasyliunas reconnection cycle, occurs in a region roughly parallel to the dawn–dusk direction and at a location that matches well the topology of the QP60 subset we discuss. Post-dusk, equatorial QP60 are clustering in a slightly wider region compared to what Cowley et al. (2005) estimates (pre-midnight sector), while this region becomes less well-defined if we include the high-latitude QP60 (Fig. 10), mainly because of large uncertainties in the field-line tracing. Despite the uncertainties, the presence of an active, post-dusk/pre-midnight local time sector is well-established by our observations and the link to the Vasyliunas reconnection cycle is worth investigating in future studies.

QP60 of the pre-dusk sector cluster near the magnetopause (Figs. 6, 7 and 10). MAG data indicate that the proximity of QP60 to the magnetopause can be a fact. The example discussed in Section 3.1.5 is such a case. Cutler et al. (2011) studied magnetometer observations from day 195 of 2007, which are consistent with KH instability taking place at the dusk flank of Saturn’s magnetopause. Inspection of LEMMS data from that period reveals several QP60, one of which is coincident with the event in Cutler et al. (2011). Finally, Delamere et al. (2013) reports several detections of KH-instability signatures between noon and dusk. KH-instability/magnetopause reconnection are also consistent with the theoretical work by Cowley et al. (2005), who predicts Dungey-cycle reconnection all the way to the dusk. The concentration of QP60 near the pre-dusk magnetopause is therefore interesting in that respect, although we cannot exclude at this point that this is coincidental and unrelated to reconnection.

4.2. Dawn magnetosphere

QP60 at the dawn magnetosphere are rare in the equatorial plane. There can be several reasons for that.

One reason is that their source is on high latitude and open field lines, meaning that the accelerated electrons escape the system before propagating to the equator. What supports this scenario is that many QP60 map poleward of the statistical aurora boundary between dawn and noon (Fig. 11). The main aurora emission is located near or at the boundary between open and closed field lines (Cowley et al., 2005; Talboys et al., 2011). Field line tracing for the QP60 poleward of the main emission also indicates that they reside on open field lines, although this result depends on the set-up of the K06 magnetic field model. Another explanation for the lack of QP60 at low latitudes could be that many events map at large distances in the tail region that Cassini has not yet sampled.

These characteristics indicate that dynamics at the magnetopause, the cusp or the tail, such as reconnection and/or KH-instability, could be associated with the QP60 on the dawnside magnetosphere. Such processes at the magnetopause and the cusp have been reported in the literature (McAndrews et al., 2008; Masters et al., 2009, 2010; Jasinski et al., 2014). Still, excluding the case discussed by Masters et al. (2010) (day 348/2004), the remaining six intervals discussed in the other three manuscripts contain no clear evidence in the LEMMS data for a simultaneous occurrence of a QP60. On the other hand, the interval analyzed by Jasinski et al. (2014) contains evidence of several B_ϕ “pulses” approximately every hour.

Solar-wind induced storms that trigger large-scale tail reconnection in the magnetotail may also be a QP60 source. The area poleward of the main auroral oval that contains many of the open-field line QP60 (Fig. 11, panels “B” and “D”), brightens significantly during such storms (Cravay et al., 2005). The enhanced brightness regions can be structured (Nichols et al., 2014) with the dark areas mapping to locations of QP60. Solar wind compression events have indeed been identified in one of the intense QP60 in the dawn magnetosphere (Example 3, Section 3.1.3) (Bunce et al., 2010). The estimated frequency of occurrence of QP60 at dawn (20–100 days – Section 3.2.1) is also not inconsistent with the scenario of solar wind induced storms.

In that respect, analysis of simultaneous aurora observations will be necessary to clarify if connection of QP60 to any of these three scenarios is viable.

4.3. QP60 as a magnetospheric electron source

In Section 3.3.2 we show two examples of energy spectra of QP60 (Fig. 14). When these are converted to phase space density as a function of μ we find that they are many orders of magnitude more intense than those of the ring current. The equatorial, post-dusk sector, at which many relativistic QP60 are seen, is at a transition region where both inflows, outflows and a considerable corotational component have been reported by Thomsen et al. (2013). This means that significant intensities of QP60 electrons may be transported by inflows to the ring current. A variety of other processes, such as diffusion, convection or large scale injections may also transport particles from the outer magnetosphere to the ring current (Kollmann et al., 2011; Andriopoulou et al., 2014; Mitchell et al., 2015). Similarities between the electron pitch angle distributions of the ring current Carbary et al. (2011) and that of a QP60 (Fig. 14) are also not against of a transport between the two regions.

A detailed assessment of the QP60 source strength requires one to also take into account the magnetospheric volume at which QP60 occur on closed field lines and compare it with the total number of energetic electrons within the ring current (Kim et al., 2000). This calculation is beyond the scope of the current study, but this initial comparison highlights that the QP60 may be a potentially

strong source of energetic electrons, which, unless equally fast and efficient loss processes act on in, it may potentially support the energetic electron population of the ring current.

4.4. 60 to 70-min period

The most commonly observed period around 60 to 70-min is puzzling, given that QP60 appear to originate from different processes and at different locations, as discussed in the earlier sections. To understand why this is unusual, we can refer to at least superficially similar, short period phenomena at Earth (termed “sawtooth events”) that are seen mostly in energetic ions and they can have periods that vary by many hours (Cai and Clauer, 2009). The terrestrial sawtooth events are attributed to periodic, large scale tail reconnection, catalyzed by a large abundance of ionospheric, oxygen ions (Brambles et al., 2011). Another type of periodic structures are the flux-transfer-events (FTE) at Earth’s dayside magnetopause, with time-scales that vary between 1 and 30 min and a mean value of 8 min (Kuo et al., 1995).

It is also useful to put in context studies of jovian quasi-periodic processes which have striking similarities with QP60 at Saturn. For instance, a 40–80 min periodicity has been observed at Jupiter in a variety of datasets, such as in energetic electrons (McKibben et al., 1993), radio waves (MacDowall et al., 1993) and the brightness of the X-ray aurora (Gladstone et al., 2002). The observations analyzed by (McKibben et al., 1993) seem to indicate a dawn–dusk asymmetry in the occurrence of quasi-periodic injections like the one we observe at Saturn.

Bunce et al. (2004) observed that the interhemispheric Alfvén wave transit time, which defines the characteristic 8-min time scale for FTEs at Earth (Kuo et al., 1995), is estimated to be between 30 and 50 min for Jupiter, close to the characteristic 40–80 min period discussed earlier. Bunce et al. (2005) applied the same calculation for Saturn using a dipole field and estimated a time scale of about 20 min for that case. Using the K06 model for a more realistic magnetic field configuration, we may reproduce the estimation by Bunce et al. (2005) and adjust it so that we can also retrieve the more common time-scale of 60 min. Overall, the results depend on the assumption we make for mean value of plasma density along the field lines (Fig. 15). More importantly, for any given density value, the time scale can change significantly for the different local time sectors of the magnetosphere that QP60 are observed (top panel). Results tend to become more uniform for a more compressed/dipolarized magnetosphere (bottom panel), but the statistical map e.g. Fig. 6 indicates that many QP60 could occur also in a significantly expanded magnetosphere. Unless there is a relation between the magnetic field and the mean plasma density that fixes the Alfvén wave time around 60-min, we cannot adopt the concept by Bunce et al. (2004) as a global solution for the problem of QP60 characteristic period.

The observations by MacDowall et al. (1993), who studied the radio-emission counterpart of the electron injections at Jupiter, indicate that their interpulse period remains rather stable, but what changes is the number of distinct pulses per event. This number was positively correlated with the magnitude of the solar wind velocity. Furthermore, Kimura et al. (2008, 2012) found that the quasi-periodic radio emissions at Jupiter are modulated at the planetary rotation period, suggesting the existence of a recurrent disturbance when a fixed planetocentric longitude range is within a certain local time sector.

What we may infer from such observations is that the interpulse period of quasi-periodic injections is defined primarily by internal characteristics of the planet’s magnetosphere and/or ionosphere, while their occurrence is modulated by the solar wind interaction. Given that the ionosphere is more uniform and stable than the outer magnetosphere, we would expect that the

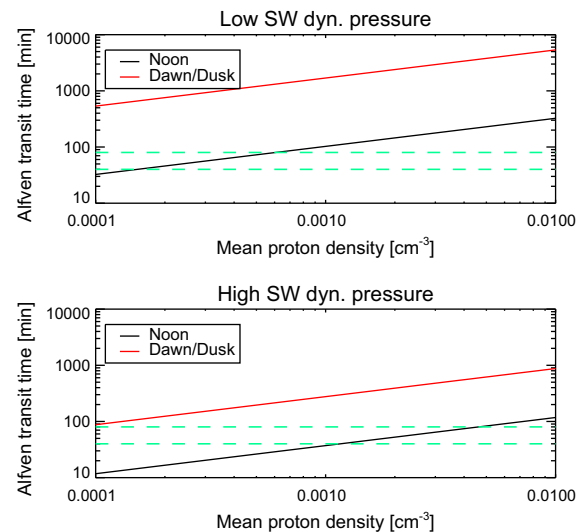


Fig. 15. The interhemispheric Alfvén wave transit time for Saturn based on the K06 magnetic field model as a function of density, magnetospheric location and solar wind dynamic pressure. The top (bottom) panel is for low (high) dynamic pressure. The green lines mark the range of interpulse periods observed for the majority of QP60. For the calculation, we assumed that the ion composition is dominated by protons. The range of density values is based on Thomsen et al. (2010). (For interpretation of the references to color in this figure legend, the reader is referred to the web version of this article.)

interpulse period is modulated by an ionospheric response to different kinds of magnetospheric transients.

Whether such characteristics are true also for Saturn will be investigated in future studies, as currently information on the upstream solar wind parameters at Saturn is limited. Finally, we did not search for rotational periodicities in our measurements, primarily because the SKR period is not well defined for times after the equinox (<http://www-pw.physics.uiowa.edu/sls4/>) when most of our QP60 events from the dusk-side magnetosphere are retrieved.

5. Summary and open questions

This work presents the first statistical analysis of short period, quasi-periodic energetic electron injections (QP60), based on nine years of energetic electron and magnetic field measurements by Cassini. Our findings indicate that QP60 are a very common feature of Saturn’s outer magnetosphere and are present almost globally. The interpulse period ranges between about 40 and 80 min, with a most typical value of about 60 min. High intensities of electrons in a QP60 can be accelerated at least up to 6 MeV, suggesting that these injections can be an efficient source of energetic electrons for the magnetosphere, and possibly for the heliosphere, as some of these observations were on open field-lines.

The asymmetry in the distribution and the properties of QP60 between dusk and dawn indicate that the origin of those events is not unique. QP60 seem to occur on regions where reconnection is theoretically expected to take place, so a potential direct or indirect link with such processes is worth investigating. More specifically, we believe that a subset of the pulsed injections at the post-dusk sector may be linked to the Vasyliunas reconnection cycle, while magnetopause reconnection/KH-instability may be considered to explain all other events at the duskside magnetosphere. QP60 at the dawnside magnetosphere may be associated to solar-wind induced storms, while magnetopause reconnection/KH-instability is a likely connection also there. If that inference is correct, QP60 may be excellent tracers for assessing the

global plasma circulation in Saturn's magnetosphere. At this stage, however, it is not possible to exclude that the collocation of QP60 with potential reconnection sites is not coincidental.

We favor an acceleration region at high-latitudes or the aurora based on earlier results by Mitchell et al. (2009) and Badman et al. (2012) and the similarities of the mapped QP60 distribution with statistical properties of Saturn's main aurora emission. A comparison with the characteristics of similar type of injections at Jupiter also points towards this direction.

Besides the aforementioned initial results, a series of outstanding questions also arise, such as what determines the rather well-defined period of 60 min, how electrons can reach up to energies of several MeV, and why escaping relativistic electrons from Saturn have not been seen in the solar wind. Extension of our QP60 dataset with the new high-latitude Cassini observations of 2013–2017, multi-instrument studies and comparison with similar observations of quasi-periodic processes at Jupiter (including the upcoming measurements by Juno) may help to provide the answers.

Acknowledgments

The German contribution of MIMI/LEMMS was in part financed by BMBF through DLR under contract 500H1101 and by the Max Planck Gesellschaft. We thank Andreas Lagg and Markus Fränz (MPS) for extensive software support, Martha Kusterer and Jon Vandegriff (both JHUAPL) for reducing the MIMI data. This work evolved also from discussions held during two meetings of the International Space Science Institute team on “Modes of Radial Transport in Magnetospheres”.

References

- Aguilar, M. et al., 2013. First result from the alpha magnetic spectrometer on the international space station: Precision measurement of the positron fraction in primary cosmic rays of 05–350 GeV. *Phys. Rev. Lett.* 110 (April). <http://dx.doi.org/10.1103/PhysRevLett.110.141102>.
- Andriopoulou, M. et al., 2014. Spatial and temporal dependence of the convective electric field in Saturn's inner magnetosphere. *Icarus* 229, 57–70. <http://dx.doi.org/10.1016/j.icarus.2013.10.028>.
- Arridge, C.S. et al., 2008. Warping of Saturn's magnetospheric and magnetotail current sheets. *J. Geophys. Res. (Space Phys.)* 113 (August), 8217. <http://dx.doi.org/10.1029/2007JA012963>.
- Badman, S.V. et al., 2012. Cassini observations of ion and electron beams at Saturn and their relationship to infrared auroral arcs. *J. Geophys. Res. (Space Phys.)* 117 (January), 1211. <http://dx.doi.org/10.1029/2011JA017222>.
- Badman, S.V. et al., 2016. Saturn's auroral morphology and field-aligned currents during a solar wind compression. *Icarus* 263, 83–93.
- Brambles, O.J. et al., 2011. Magnetosphere sawtooth oscillations induced by ionospheric outflow. *Science* 332 (June), 1183. <http://dx.doi.org/10.1126/science.1202869>.
- Bunce, E.J., Cowley, S.W.H., Yeoman, T.K., 2004. Jovian cusp processes: Implications for the polar aurora. *J. Geophys. Res. (Space Phys.)* 109 (A9). <http://dx.doi.org/10.1029/2003JA010280>, n/a–n/a.
- Bunce, E.J., Cowley, S.W.H., Milan, S.E., 2005. Interplanetary magnetic field control of Saturn's polar cusp aurora. *Ann. Geophys.* 23 (June), 1405–1431.
- Bunce, E.J. et al., 2010. Extraordinary field-aligned current signatures in Saturn's high-latitude magnetosphere: Analysis of Cassini data during Revolution 89. *J. Geophys. Res. (Space Phys.)* 115 (October), 10238. <http://dx.doi.org/10.5194/angeo-23-1405-2005>.
- Cai, X., Clauer, C.R., 2009. Investigation of the period of sawtooth events. *J. Geophys. Res. (Space Phys.)* 114 (A6). <http://dx.doi.org/10.1029/2008JA013764>, n/a–n/a.
- Carbary, J.F., 2012. The morphology of Saturn's ultraviolet aurora. *J. Geophys. Res. (Space Phys.)* 117 (A6). <http://dx.doi.org/10.1029/2012JA017670>, n/a–n/a.
- Carbary, J.F. et al., 2011. Pitch angle distributions of energetic electrons at Saturn. *J. Geophys. Res. (Space Phys.)* 116 (January), 1216. <http://dx.doi.org/10.1029/2010JA015987>.
- Cowley, S.W.H. et al., 2005. Reconnection in a rotation-dominated magnetosphere and its relation to Saturn's auroral dynamics. *J. Geophys. Res. (Space Phys.)* 110 (February), 2201.
- Crary, F.J. et al., 2005. Solar wind dynamic pressure and electric field as the main factors controlling Saturn's aurorae. *Nature* 433 (February), 720–722. <http://dx.doi.org/10.1038/nature03333>.
- Cutler, J.C. et al., 2011. Evidence of surface wave on the dusk flank of Saturn's magnetopause possibly caused by the Kelvin–Helmholtz instability. *J. Geophys. Res. (Space Phys.)* 116 (A10). <http://dx.doi.org/10.1029/2011JA016643>, n/a–n/a.
- de Pater, I., 1981. A comparison of radio data and model calculations of Jupiter's synchrotron radiation 2. East–west asymmetry in the radiation belts as a function of jovian longitude. *J. Geophys. Res.* 86 (May), 3423–3429. <http://dx.doi.org/10.1029/JA086iA05p03423>.
- Delamere, P.A. et al., 2013. Magnetic signatures of Kelvin–Helmholtz vortices on Saturn's magnetopause: Global survey. *J. Geophys. Res. (Space Phys.)* 118 (January), 393–404. <http://dx.doi.org/10.1029/2012JA018197>.
- Dougherty, M.K. et al., 2004. The Cassini magnetic field investigation. *Space Sci. Rev.* 114 (September), 331–383. <http://dx.doi.org/10.1007/s11214-004-1432-2>.
- Gannon, J.L., Li, X., Temerin, M., 2005. Parametric study of shock-induced transport and energization of relativistic electrons in the magnetosphere. *J. Geophys. Res. (Space Phys.)* 110 (December), 12206. <http://dx.doi.org/10.1029/2004JA010679>.
- Gladstone, G.R. et al., 2002. A pulsating auroral X-ray hot spot on Jupiter. *Nature* 415 (February), 1000–1003. <http://dx.doi.org/10.1038/4151000a>.
- Grodent, D., Waite Jr., J.H., Gérard, J.-C., 2001. A self-consistent model of the jovian auroral thermal structure. *J. Geophys. Res.* 106 (July), 12933–12952. <http://dx.doi.org/10.1029/2000JA000129>.
- Gurnett, D.A. et al., 2010. A plasmopause-like density boundary at high latitudes in Saturn's magnetosphere. *Geophys. Res. Lett.* 37 (August), 16806. <http://dx.doi.org/10.1029/2010GL044666>.
- Horne, R.B. et al., 2005. Wave acceleration of electrons in the Van Allen radiation belts. *Nature* 437 (September), 227–230. <http://dx.doi.org/10.1038/nature03939>.
- Jasinski, J.M. et al., 2014. Cusp observation at Saturn's high-latitude magnetosphere by the Cassini spacecraft. *Geophys. Res. Lett.* 41 (5), 1382–1388. <http://dx.doi.org/10.1002/2014GL059319>.
- Kanani, S.J. et al., 2010. A new form of Saturn's magnetopause using a dynamic pressure balance model, based on in situ, multi-instrument Cassini measurements. *J. Geophys. Res. (Space Phys.)* 115 (June), 6207. <http://dx.doi.org/10.1029/2009JA014262>.
- Khurana, K.K., 1997. Euler potential models of Jupiter's magnetospheric field. *J. Geophys. Res.* 102 (June), 11295–11306. <http://dx.doi.org/10.1029/97JA00563>.
- Khurana, K.K. et al., 2006. A model of Saturn's magnetospheric field based on latest Cassini observations. AGU Meeting (Spring). Abstracts A1.
- Kim, H.-J. et al., 2000. Can substorms produce relativistic outer belt electrons? *J. Geophys. Res. (Space Phys.)* 105 (A4), 7721–7735. <http://dx.doi.org/10.1029/1999JA000465>.
- Kimura, T. et al., 2012. Polarization and direction of arrival of jovian quasiperiodic bursts observed by Cassini. *J. Geophys. Res. (Space Phys.)* 117 (November), 11209. <http://dx.doi.org/10.1029/2012JA017506>.
- Kimura, T. et al., 2008. Radiation characteristics of quasi-periodic radio bursts in the jovian high-latitude region. *Planet. Space Sci.* 56 (December), 1967–1976. <http://dx.doi.org/10.1016/j.pss.2008.09.021>.
- Kollmann, P. et al., 2011. Energetic particle phase space densities at Saturn: Cassini observations and interpretations. *J. Geophys. Res. (Space Phys.)* 116 (May), A05222. <http://dx.doi.org/10.1029/2010JA016221>.
- Krimigis, S.M. et al., 2004. Magnetosphere Imaging Instrument (MIMI) on the Cassini Mission to Saturn/Titan. *Space Sci. Rev.* 114 (September), 233–329. <http://dx.doi.org/10.1007/s11214-004-1410-8>.
- Krupp, N. et al., 2009. Energetic particles in Saturn's magnetosphere during the Cassini nominal mission (July 2004–July 2008). *Planet. Space Sci.* 57 (December), 1754–1768. <http://dx.doi.org/10.1016/j.pss.2009.06.010>.
- Kuo, H., Russell, C.T., Le, G., 1995. Statistical studies of flux transfer events. *J. Geophys. Res. (Space Phys.)* 100 (A3), 3513–3519. <http://dx.doi.org/10.1029/94JA02498>.
- Lamy, L. et al., 2010. Properties of Saturn Kilometric Radiation measured within its source region. *Geophys. Res. Lett.* 37 (June), 12104. <http://dx.doi.org/10.1029/2010GL043415>.
- Lyons, L.R., Thorne, R.M., 1973. Equilibrium structure of radiation belt electrons. *J. Geophys. Res.* 78 (May), 2142–2149.
- MacDowell, R.J. et al., 1993. Quasiperiodic jovian radio bursts: Observations from the Ulysses radio and plasma wave experiment. *Planet. Space Sci.* 41 (November), 1059–1072. [http://dx.doi.org/10.1016/0032-0633\(93\)90109-F](http://dx.doi.org/10.1016/0032-0633(93)90109-F).
- Masters, A. et al., 2009. Surface waves on Saturn's dawn flank magnetopause driven by the Kelvin–Helmholtz instability. *Planet. Space Sci.* 57 (December), 1769–1778. <http://dx.doi.org/10.1016/j.pss.2009.02.010>.
- Masters, A. et al., 2010. Cassini observations of a Kelvin–Helmholtz vortex in Saturn's outer magnetosphere. *J. Geophys. Res. (Space Phys.)* 115 (July), 7225. <http://dx.doi.org/10.1029/2010JA015351>.
- Mauk, B.H., Fox, N.J., 2010. Electron radiation belts of the Solar System. *J. Geophys. Res. (Space Phys.)* 115 (December), 12220. <http://dx.doi.org/10.1029/2010JA015660>.
- Mauk, B.H. et al., 2005. Energetic particle injections in Saturn's magnetosphere. *Geophys. Res. Lett.* 32 (June), 14. <http://dx.doi.org/10.1029/2005GL022485>.
- McAndrews, H.J. et al., 2008. Evidence for reconnection at Saturn's magnetopause. *J. Geophys. Res. (Space Phys.)* 113 (April), 4210. <http://dx.doi.org/10.1029/2007JA012581>.
- McKibben, R.B., Simpson, J.A., Zhang, M., 1993. Impulsive bursts of relativistic electrons discovered during Ulysses' traversal of Jupiter's dusk-side magnetosphere. *Planet. Space Sci.* 41 (November), 1041–1058. [http://dx.doi.org/10.1016/0032-0633\(93\)90108-E](http://dx.doi.org/10.1016/0032-0633(93)90108-E).

- Mitchell, D.G. et al., 2009. Ion conics and electron beams associated with auroral processes on Saturn. *J. Geophys. Res. (Space Phys.)* 114 (February), 2212. <http://dx.doi.org/10.1029/2008JA013621>.
- Mitchell, D.G. et al., 2016. Recurrent pulsations in Saturn's high latitude magnetosphere. *Icarus* 263, 94–100.
- Mitchell, D.G. et al., 2015. Injection, interchange and reconnection. In: Keiling, A., Jackman, C.M., Delamere, P.A. (Eds.), *Magnetotails in the Solar System*. John Wiley & Sons Inc, Hoboken, NJ. <http://dx.doi.org/10.1002/9781118842324.ch19>.
- Nichols, J.D. et al., 2014. Dynamic auroral storms on Saturn as observed by the hubble space telescope. *Geophys. Res. Lett.* 41 (10), 3323–3330. <http://dx.doi.org/10.1002/2014GL060186>.
- Paranicas, C. et al., 2010. Transport of energetic electrons into Saturn's inner magnetosphere. *J. Geophys. Res. (Space Phys.)* 115 (September), 9214. <http://dx.doi.org/10.1029/2010JA015853>.
- Radioti, A. et al., 2011. Bifurcations of the main auroral ring at Saturn: Ionospheric signatures of consecutive reconnection events at the magnetopause. *J. Geophys. Res. (Space Phys.)* 116 (November), 11209. <http://dx.doi.org/10.1029/2011JA016661>.
- Radioti, A. et al., 2013. Auroral signatures of multiple magnetopause reconnection at Saturn. *Geophys. Res. Lett.* 40 (September), 4498–4502. <http://dx.doi.org/10.1002/grl.50889>.
- Roussos, E. et al., 2011. Long- and short-term variability of Saturn's ionic radiation belts. *J. Geophys. Res. (Space Phys.)* 116 (February), A02217. <http://dx.doi.org/10.1029/2010JA015954>.
- Saur, J. et al., 2006. Anti-planetward auroral electron beams at Saturn. *Nature* 439 (February), 699–702. <http://dx.doi.org/10.1038/nature04401>.
- Schardt, A.W. et al., 1985. Particle acceleration in Saturn's outer magnetosphere – In memoriam Alois Schardt. *J. Geophys. Res.* 90 (September), 8539–8542. <http://dx.doi.org/10.1029/JA090iA09p08539>.
- Shprits, Y.Y. et al., 2012. Gyroresonant interactions between the radiation belt electrons and whistler mode chorus waves in the radiation environments of Earth, Jupiter, and Saturn: A comparative study. *J. Geophys. Res. (Space Phys.)* 117 (November), 11216. <http://dx.doi.org/10.1029/2012JA018031>.
- Talboys, D.L. et al., 2011. Statistical characteristics of field-aligned currents in Saturn's nightside magnetosphere. *J. Geophys. Res. (Space Phys.)* 116 (April), 4213. <http://dx.doi.org/10.1029/2010JA016102>.
- Thomsen, M.F. et al., 2010. Survey of ion plasma parameters in Saturn's magnetosphere. *J. Geophys. Res. (Space Phys.)* 115 (A10). <http://dx.doi.org/10.1029/2010JA015267>, n/a–n/a.
- Thomsen, M.F. et al., 2013. Cassini/CAPS observations of duskside tail dynamics at Saturn. *J. Geophys. Res. (Space Phys.)* 118 (September), 5767–5781. <http://dx.doi.org/10.1002/jgra.50552>.
- Thorne, R.M., 1983. Microscopic plasma processes in the jovian magnetosphere. In: Dessler, A.J. (Ed.), *Physics of the Jovian Magnetosphere*. Cambridge Planetary Science Old (No. 3). Cambridge University Press, Cambridge, pp. 454–488. <http://dx.doi.org/10.1017/CBO9780511564574.014>.
- Walker, R.J. et al., 2011. A simulation study of Kelvin–Helmholtz waves at Saturn's magnetopause. *J. Geophys. Res. (Space Phys.)* 116 (March), 3203. <http://dx.doi.org/10.1029/2010JA015905>.
- Zhang, M. et al., 1995. Impulsive bursts of energetic particles in the high-latitude duskside magnetosphere of Jupiter. *J. Geophys. Res.* 100 (October), 19497–19512. <http://dx.doi.org/10.1029/95JA02099>.